A CuZn-BTC derived stable Cu/ZnO@SiO$_2$ catalyst for ethanol dehydrogenation

Haolan Liu [a], Zhili Chang [a], Jie Fu [b], Zhaoyin Hou [a,c,*]

[a] Key Laboratory of Biomass Chemical Engineering of Ministry of Education, Department of Chemistry, Zhejiang University, Hangzhou 310028, China
[b] Key Laboratory of Biomass Chemical Engineering of Ministry of Education, College of Chemical & Biological Engineering, Zhejiang University, Hangzhou 310027, China
[c] Center of Chemistry for Frontier Technologies, Department of Chemistry, Zhejiang University, Hangzhou 310028, China

ARTICLE INFO

ABSTRACT

Cu-based catalysts play pivotal role in many industrial processes, however, its application under high temperature is restricted due to the low Tammann temperature of Cu. Improving the stability and activity of Cu-based catalysts at high temperature is a challenge. In this work, a stable Cu/ZnO@SiO$_2$ catalyst was prepared, in which silicon was introduced into CuZn-BTC precursor via a steam-assisted hydrolysis method before calcination and reduction. Characterizations found that Cu/ZnO@SiO$_2$ catalyst prepared via above strategy possesses increased surface area, more exposed active sites and excellent stability for ethanol dehydrogenation than Cu/ZnO (prepared from CuZn-BTC without SiO$_2$). It was confirmed that the space-time yield of acetaldehyde reached 9.0 g-acetaldehyde/g-cat/h, and Cu/ZnO@SiO$_2$ could maintain its activity within 200 h at 350 °C due to the ZnO decorated Cu particles (Cu/ZnO) were encapsulated in the octahedral shaped SiO$_2$ hollow.

1. Introduction

Ethanol is an important feedstock for its huge amount of productivity, renewable and low price. It was estimated that the productivity of bio-ethanol has reached 8×10^{10} liters in 2017, and catalytic upgrading of ethanol to valuable chemicals became a hot topic in the past decade [1–3]. Among of them, dehydrogenation of ethanol to acetaldehyde is an industrially interesting process that attracts the attention of many scientists [4–6], which might be attributed to that acetaldehyde is an important intermediate and is currently manufactured via environmental unfriendly Wacker-Hoechst process in the presence of a homogeneous PdCl$_2$/CuCl$_2$ catalyst in liquid-phase [7,8]. At the same time, the only by-product in the dehydrogenation of ethanol to acetaldehyde is hydrogen, which will make this process green, economical and sustainable.

In the past decade, Cu-based catalysts were recommended popularly for the dehydrogenation of ethanol for its high activity, selectivity and low price [9–13]. These works provided very important founding and insights on the reaction mechanism and structure-performance relationship of Cu-based catalysts for dehydrogenation of ethanol. However, dehydrogenation of ethanol is an endothermic process (see the following Eq. (1)) [13–15], and high temperature is more favorable to increase the

conversion of ethanol in single pass.

$$CH_3CH_2OH \rightarrow CH_3CHO + H_2 \ (\Delta H = 71 \cdot 85 \text{ kJ/mol, } 300 \text{ °C}) \tag{1}$$
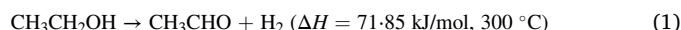
Unfortunately, Cu nanoparticles (NPs) agglomerate easily at high temperature due to the low Tammann temperature of Cu (405 °C) [16, 17]. Improving the stability and activity of Cu-based catalysts is a challenge for those reactions which might be carried out at high temperature. In the published works, several strategies have been developed in order to retard the growth of Cu NPs during the dehydrogenation of ethanol, these methods include using specific support (e.g. carbon materials [18], ZnO [19], Cr$_2$O$_3$ [20]), or alloying Cu with refractory metals (e.g. Ni [21], Pt [22]), or immobilization Cu in framework of hierarchical MFI [23] or encapsulated Cu within silicalite-1 [24]. And these approaches have made significant progresses, however, the stability and activity of Cu-based catalysts at high temperature (over 300 °C) remains a challenge.

Metal-organic frameworks (MOFs) possess highly ordered porous structure, uniform pore channels and high surface areas [25,26]. Metal ions that locate at the nodes of MOF dispersed homogenously and can work in synergy with encapsulated NPs [27–30]. At the same time, MOFs can also be used as self-sacrificing templates toward the

---

fabrication of special structured catalysts. It was confirmed that MOF-derived metal NPs, alloy and/or oxides benefit from the precise morphologies and hierarchical porosities, and serve as excellent and durable heterogeneous catalysts for a variety of reactions [31–34]. Previous works in our laboratory found that a Cu(Zn)-BTC precursor derived Cu/ZnO catalyst with nano sized ZnO dotted on Cu particles was extremely active and stable for hydrogenolysis of glycerol due to the enlarged interface between Cu and ZnO [31]. But the direct calcination of MOFs precursor is a violent exothermic process, and thus, the surface area of synthesized metal NPs and/or oxides is low because of sintering [31,33].

Here, a stable Cu-based catalyst with increased surface area was synthesized via a controlled decomposition and reduction of a silica encapsulated CuZn-BTC. The structure and properties of the precursor and catalyst were characterized with various techniques. The prominent performance of the catalyst under varied conditions and the stability at high temperature were evaluated in detail.

2. Experimental

2.1. Materials

$Cu(NO_3)_2 \cdot 3H_2O$, ZnO, N,N′-dimethylformamide (DMF) and ethanol were purchased from Sinopharm Chemical Reagent Co., Ltd (Shanghai, China). Tetraethyl orthosilicate (TEOS) was obtained from Aladdin Biochemical Technology Co., Ltd (Shanghai, China). 1,3,5-benzenetri-carboxylic acid (H_3BTC) was purchased from Energy chemical. All the reagents and solvents were used as received without further purification.

2.2. Catalysts preparation

2.2.1. Preparation of CuZn-BTC

CuZn-BTC was prepared in a rapid method at room temperature according to reference [35]. And the procedures were addressed in Supporting information section in detail.

2.2.2. Preparation of CuZn^{BTC}@SiO$_2$

SiO$_2$ encapsulated CuZn-BTC was synthesized via a steam-assisted hydrolysis process. At first, the as-synthesized CuZn-BTC (2.4 g) was degassed at 100 °C in vacuum ($< 10^{-7}$ Pa) for 6 h. And then, the system in vacuum was cooled to room temperature, and 15 mL TEOS was added to above pretreated CuZn-BTC. After that, the mixture was sonicated for 15 min and maintained overnight at room temperature in order to make the pore channels of CuZn-BTC full of TEOS, the precursor sediment was filtered. Subsequently, the solid was transferred to a small beaker and the beaker was placed in a Teflon-lined autoclave with 20 mL H$_2$O (see Fig. S1). The steam-assisted hydrolysis was performed at 110 °C for 12 h. Finally, the solid was dried at 80 °C in a vacuum for overnight and denoted as CuZn^{BTC}@SiO$_2$.

2.2.3. Preparation of CuZnO@SiO$_2$

CuZnO@SiO$_2$ was prepared via the controlled calcination of above prepared CuZn^{BTC}@SiO$_2$ in air flow (30 mL/min) at 400 °C for 4 h with a ramp of 2 °C/min.

2.2.4. Preparation of Cu/ZnO@SiO$_2$

Before catalytic reaction, the calcined CuZnO@SiO$_2$ was pressed into granular (40–60 mesh), and then reduced at 350 °C in 5% H$_2$/N$_2$ flow (60 mL/min) for 1 h. The reduced catalyst was denoted as Cu/ZnO@-SiO$_2$. These procedures were diagrammatically depicted in Scheme 1.

2.2.5. Preparation of reference catalysts

Cu/ZnO catalyst without SiO$_2$ hollow was prepared via the direct calcination and reduction of CuZn-BTC according to the reference [35], and these procedures were addressed in Supporting information section.
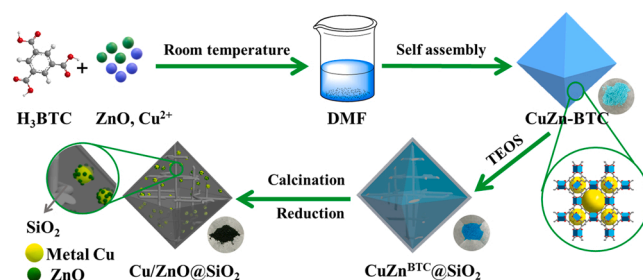
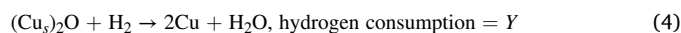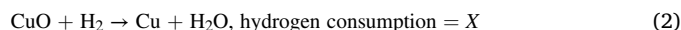**Scheme 1.** Schematic illustration of the preparation of Cu/ZnO@SiO$_2$.

As references, Cu@SiO$_2$ and ZnO@SiO$_2$ catalysts were prepared in the same method, and preparation procedures for these catalysts were described in detail in Supporting information.

2.3. Characterizations

X-ray diffraction (XRD) patterns were recorded on a Rigaku Smar-tLab diffractometer using Cu $K\alpha$ radiation ($\lambda = 1.5406$ Å) at 40 kV and 180 mA. N$_2$ adsorption-desorption isotherms were measured using an ASAP 2010 analyzer (Micromeritics) after degasification at 100 °C for 6 h in vacuum. The Brunner-Emmet-Teller (BET) surface area was calculated according to the adsorption branch in the range of p/p_0 = 0.005–0.1 (for CuZn-BTC and CuZn^{BTC}@SiO$_2$) or 0.05–0.30 (for other samples). Thermogravimetric and differential scanning calorimeter (TG-DSC) analysis were performed on a Netzsch STA 409 thermoanalyzer with a heating rate of 2 °C/min in air flow (30 mL/min) from room temperature to 500 °C. Fourier-transfer infrared spectroscopic (FT-IR) analysis was carried on a Nicolet Is10 FTIR spectrometer using KBr method in 400–4000 cm^{-1}. X-ray photoelectron spectroscopy (XPS) spectra were detected on a Kratos Axis Ultra DLD system, and the X-ray source was standard Mg anode (1253.6 eV). Scanning electron micro-scopy (SEM) images were obtained on Hitachi SU8010 at 5 kV, and samples were sprayed with platinum in order to avoid charging. Transmission electron microscope (TEM) images and high angle angular dark field-scanning transmission electron microscopy (HAADF-STEM) images of these catalysts were obtained on JEOL-2020F at an acceler-ating voltage of 200 kV. Line-scan elemental energy-dispersive spec-trometry (EDS) analysis was carried out with an FEI TECNAI F30 microscope at 200 kV.

H$_2$ temperature-programmed reduction (H$_2$-TPR) experiments were carried out in the following procedures: samples (30 mg) were first pretreated at 450 °C for 1 h in Ar flow (30 mL/min) and cooled to 50 °C. Then, 10 % H$_2$/N$_2$ mixture was shifted to the reactor and the reactor was heated to 450 °C with a heating rate of 10 °C/min. The effluent gas was monitored with an online quadrupole mass spectrometer (OmniStarTM, GSD301, Switzerland).

N$_2$O oxidation and followed H$_2$ titration was carried out in the following procedure, (i) calcined samples were first reduced in the same procedures as above H$_2$-TPR and the consumption of hydrogen (denoted as *X*) was recorded. (ii) The reactor was then cooled to 30 °C in purified Ar. (iii) 20% N$_2$O/Ar was introduced to the catalyst for 60 min in order to make all surface Cu (denoted as Cu$_s$) oxidized. (iv) The reactor was purged with Ar for 120 min in order to remove all N$_2$O in reactor. (v) Another H$_2$-TPR process was performed again, and the consumption of hydrogen was denoted as *Y*.

$$CuO + H_2 \rightarrow Cu + H_2O, \text{ hydrogen consumption} = X \qquad (2)$$

$$2Cu_s + N_2O \rightarrow (Cu_s)_2O + N_2 \qquad (3)$$

$$(Cu_s)_2O + H_2 \rightarrow 2Cu + H_2O, \text{ hydrogen consumption} = Y \qquad (4)$$

The dispersion of Cu was calculated as:

$$D = (2 \times Y/X) \times 100 \% \qquad (5)$$

The area of surface Cu_s was calculated as:

$$S = 2 \times Y \times N_{av}/(X \times M_{Cu} \times 1.4 \times 10^{19}) = 1353 \times Y/X \ (m^2\text{-}Cu/g\text{-}Cu) \quad (6)$$

N_{av} is the Avogadro's constant and M_{Cu} is the relative atomic mass of copper (63.5 g/mol) in these equations.

2.4. Catalytic reaction

Catalytic reaction was performed in a vertical fixed-bed reactor at atmospheric pressure. Catalyst (0.3 g, sized in 40–60 mesh) was packed in the middle of quartz tube reactor (*I.D.* = 8 mm, *L* = 270 mm), both sides of the reactor were sealed with quartz sand. Before reaction, catalyst was reduced at 350 °C for 1 h with 5% H_2/N_2 (60 mL/min), and it was cooled to desired temperature. Ethanol was fed into the reactor continuously using a high-pressure pump (Shimadzu, LC-20AD) with 20 mL/min purified nitrogen (99.99%, as the carrier gas and internal standard). The effluent gas from the reactor was cooled in a cold trap (kept at −25 °C), and the liquid products were selected, weighted and analyzed with a gas chromatograph (GC, Shimadzu, 14B) equipped with a flame ionization detector and a 30 m capillary column (DB-WAX 52 CB, USA). The gaseous products (such as H_2) were detected using an online GC (Schimadzu, 8 A) with a TCD detector and a Porapack Q column. The conversion of ethanol and the selectivity of each product were calculated based on the following equations:

$$Conv \cdot (\%) = (N_{in(ethanol)}\text{-}N_{out(ethanol)})/N_{in(ethanol)} \times 100\% \quad (7)$$

$$S_{AcH} \ (\%) = N_{(AcH)}/(N_{in(ethanol)}\text{-}N_{out(ethanol)}) \times 100\% \quad (8)$$

3. Results and discussion

3.1. The properties of CuZn-BTC and CuZn^BTC@SiO_2 precursors

XRD patterns of CuZn-BTC and $CuZn^{BTC}@SiO_2$ precursors were presented in Fig. 1(a). It was confirmed that well-structured $(CuZn)_3(BTC)_2$ formed in CuZn-BTC, and it exhibited the same diffraction patterns as the typical $Cu_3(BTC)_2$ (JCPDS 00–064–0936) because of the similar radius of Cu^{2+} (7.2 Å) and Zn^{2+} (7.4 Å) [36]. And it was interesting to note that the intensity of these diffraction peaks of $CuZn^{BTC}@SiO_2$ was lower, which might be attributed to the accumulation of SiO_2 on CuZn-BTC. But the primary profiles and the relative intensities of these diffraction peaks of $CuZn^{BTC}@SiO_2$ were similar as that of $Cu_3(BTC)_2$, which manifested that the framework of CuZn-BTC remained even after the introduction of SiO_2. At the same time, the calculated cell parameters of CuZn-BTC and $CuZn^{BTC}@SiO_2$ (a=b=c=2.644 nm, see Table S1) fitted well with the data of typical $Cu_3(BTC)_2$ that reported in literature (2.643 nm) [37].

FTIR spectra of CuZn-BTC and $CuZn^{BTC}@SiO_2$ were compared in Fig. 1(b). The C=C stretching in benzene ring (1375 cm^{-1}), the C=O stretching vibration of trimesic acid (1647 cm^{-1}) and the scissoring vibration of the carboxylate ion (730 cm^{-1}) appeared clearly and fitted well with the previously reported $Cu_3(BTC)_2$ structure in literature [38]. Apart from the typical signals of $Cu_3(BTC)_2$, another three peaks appeared at 1095, 934 and 870 cm^{-1} in $CuZn^{BTC}@SiO_2$, which were attributed to the characteristic vibrations of Si-O-Si groups [39]. These results confirmed that SiO_2 was successfully introduced in the framework of CuZn-BTC.

N_2 adsorption isotherms of both samples were classical type I model with obvious N_2 uptake in the range of 0.0–0.03 of p/p_0 (see Fig. 1(c)), indicating the presence of micropores. Fig. 1(d) further confirmed that CuZn-BTC possesses double microporous pores that sized in 0.73 and
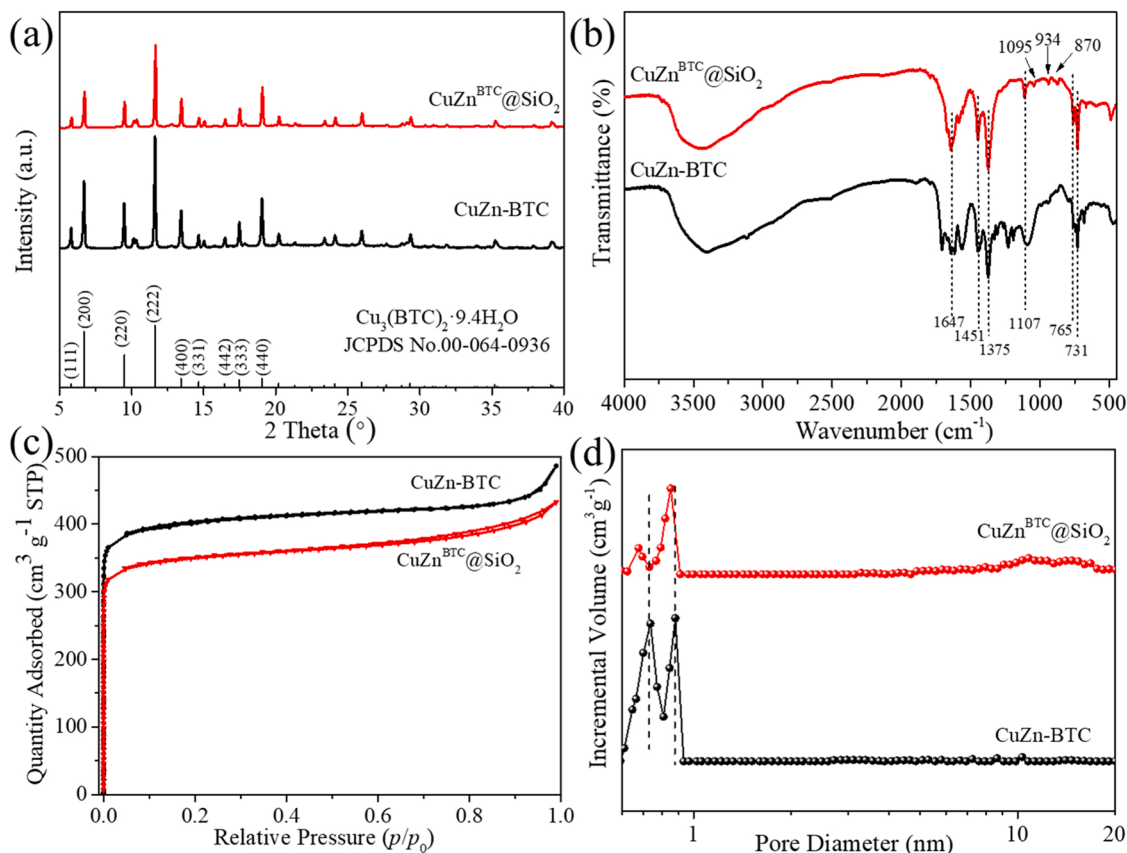

Fig. 1. XRD (a), FTIR (b), N_2 adsorption-desorption isotherms (c) and pore size distribution (d) of CuZn-BTC and $CuZn^{BTC}@SiO_2$.

0.87 nm, respectively, which was consistent with previous literatures [40]. On the other hand, the diameter of these pore channels decreased to 0.67 and 0.83 nm when SiO_2 was introduced in $CuZn^{BTC}@SiO_2$. This decreased diameter might be attributed to that SiO_2 would penetrate the pore channels of CuZn-BTC. The calculated surface area and pore volume of $CuZn^{BTC}@SiO_2$ also decreased from 1606 m^2/g and 0.55 cm^3/g (of CuZn-BTC) to 1202 m^2/g and 0.42 cm^3/g, respectively (see Table S1). These results further indicated that SiO_2 was effectively introduced into the channels and/or the surface of CuZn-BTC.

Fig. 2 compared the TG analysis results of CuZn-BTC and $CuZn^{BTC}@SiO_2$ in air flow. It was found that there were three mass loss stages during the calcination of both samples. The first stage at 25–150 °C was ascribed to the volatilization of adsorbed water or solvent, and the second mass loss between 150 and 300 °C might result from the decomposition of organic linkers at the edge of CuZn-BTC. After that, organic linkers in CuZn-BTC began to burning violently accompanied with two huge exothermic peaks at around 318.4 and 333.8 °C [41]. Compared with CuZn-BTC, the burning of organic linkers in $CuZn^{BTC}@SiO_2$ delayed to 358.4 °C and the decomposition process became gentler in the temperature ranged from 320 to 365 °C. These results indicated that the introduction of SiO_2 (or the coating of SiO_2 outside CuZn-BTC) could prevent the violent burning of organic linkers. That is, the stability of the CuZn-BTC could be improved after the introduction of SiO_2. According to the total mass loss before 500 °C, the calculated mass ratio of SiO_2 in the final $CuZnO@SiO_2$ is 23.8 wt%.

Fig. 3 exhibited the typical SEM images and surface morphologies of CuZn-BTC and $CuZn^{BTC}@SiO_2$. It can be found that pristine CuZn-BTC had a typical regular octahedral profile with a clear surface, and the corresponding EDS analysis confirmed Cu and Zn dispersed uniformly in the particles. It is interesting to find that the octahedral outline remained well in $CuZn^{BTC}@SiO_2$, but the surface of these octahedrons became rough because of the introduction of SiO_2, which made the clear CuZn-BTC particles covered. EDS analysis further disclosed that the content of Si, Cu and Zn changed simultaneously in the octahedral $CuZn^{BTC}@SiO_2$ particles.
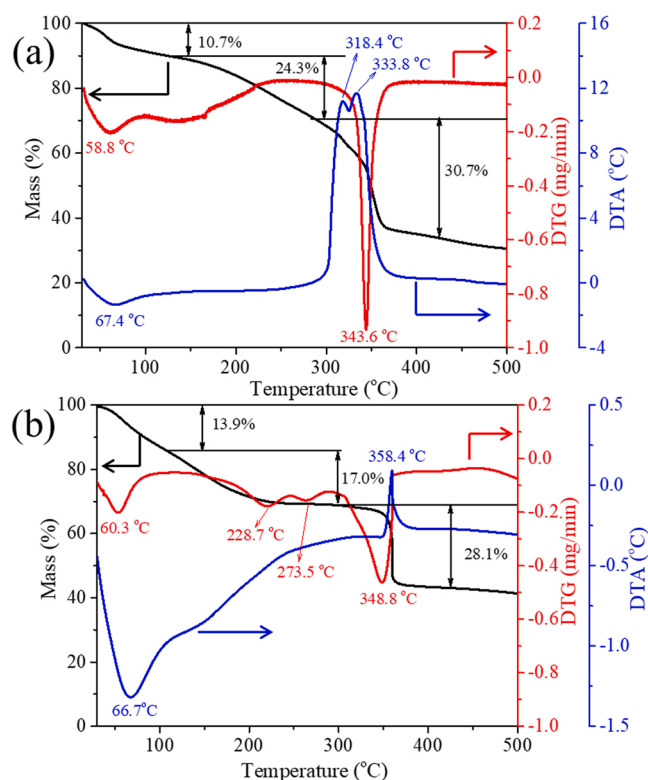

Fig. 2. Thermal analysis of CuZn-BTC (a) and $CuZn^{BTC}@SiO_2$ (b).

3.2. The properties of calcined $CuZnO@SiO_2$

Fig. 4(a) showed the XRD patterns of calcined $CuZnO@SiO_2$ and compared with the reference CuZnO that prepared via the direct calcination of CuZn-BTC (without SiO_2). Obvious CuO phase (JCPDS 00–048–1548) with three typical peaks at $2\theta = 43.4°$, 50.4° and 74.1° was detected in both samples. Meanwhile, the board peak in 19–25° in $CuZnO@SiO_2$ might be attributed to the signal of amorphous silica. But it was interesting to note that the characteristic reflections of CuO in $CuZnO@SiO_2$ became weaker and the calculated crystalline size of CuO also decreased from 14.6 nm (in CuZnO) to 3.9 nm. These results suggested that the introduction of SiO_2 could make the burning of organic linkers gentler (see Fig. 2) and depress the sintering of CuO particles during the calcination process.

At the same time, N_2 adsorption-desorption analysis further disclosed that the surface area of $CuZnO@SiO_2$ reached 139.7 m^2/g, which is 25 times higher than that of CuZnO (5.3 m^2/g) (see Fig. 4(b) and Table 1). The pore volume of $CuZnO@SiO_2$ reached 0.33 cm^3/g which is higher than that of CuZnO (0.02 cm^3/g). Once again, these data inferred that SiO_2 could prevent the violently collapse of CuZn-BTC's framework and depress the sintering of CuO and/or ZnO during calcination.

Fig. S2 compared H_2-TPR profiles of calcined CuZnO and $CuZnO@$-SiO_2. There was only one reduction peak in both samples, which could be attributed to the reduction of Cu^{2+} to Cu^0 and/or Cu^+ [42]. But the reduction temperature increased obviously from 215 °C (in CuZnO) to 245 °C (in $CuZnO@SiO_2$) when SiO_2 was introduced, indicating that CuO species in $CuZnO@SiO_2$ were more stable.

N_2O titration and followed H_2 reduction analysis further disclosed that the dispersion of Cu in $CuZnO@SiO_2$ reached to 20.4%, which was several times higher than that of CuZnO (3.5%, without SiO_2) that was prepared via the direct calcination of pristine CuZn-BTC [35]. Meanwhile, the calculated average diameter of Cu in reduced $CuZnO@SiO_2$ and CuZnO was 4.9 and 22.2 nm, respectively. The higher dispersion of Cu in $CuZnO@SiO_2$ might be attributed to that SiO_2 prevented the sintering of CuO and the larger surface area of $CuZnO@SiO_2$ (see Fig. 4).

XPS survey spectra of CuZnO and $CuZnO@SiO_2$ was shown in Fig. S3, and the obvious signals of Si 2p were detected in $CuZnO@SiO_2$. At the same time, high-resolved Cu 2p spectrum (Fig. 5) indicated that the binding energy of Cu $2p_{3/2}$ and Cu $2p_{1/2}$ shifted from 933.9 and 953.6 eV (in CuZnO) to 934.4 and 954.2 eV (in $CuZnO@SiO_2$), indicating that the interaction between Cu and ZnO (and/or between Cu and SiO_2) became stronger after the introduction of SiO_2. The binding energy at 942–944 eV in the XPS spectrum is attributed to the satellite of Cu^{2+}. After reduction, the overall binding energy of Cu $2p_{3/2}$ and Cu $2p_{1/2}$ decreased to 932.9 and 952.8 eV, respectively, because of the formation metallic Cu and/or Cu^+. The existence of Cu^0 in reduced $Cu/ZnO@SiO_2$ was also confirmed via Cu LMM auger spectra (see Fig. S4). The calculated mol ratio of Cu^0 to Cu^+ in $Cu/ZnO@SiO_2$ was 1.25, which might be attributed to the strong interaction between Cu and SiO_2. And the synergism between Cu^+ and Cu^0 would improve the activity of $Cu/ZnO@SiO_2$ [23]. It is worth noting that the surface content of Cu in $CuZnO@SiO_2$ was lower than the bulk content (see Table 1), which might be attributed to that Cu and/or ZnO species was covered by the added SiO_2.

3.3. The properties of reduced $Cu/ZnO@SiO_2$

Fig. S5 displayed the XRD pattern of reduced $Cu/ZnO@SiO_2$ and compared with the reference Cu/ZnO (without SiO_2). It was found that mainly metallic Cu (JCPDS 01–085–1326) and ZnO (JCPDS 00–065–0725) were detected in both samples. At the same time, the calculated crystalline size of Cu in these catalysts was 4.0 nm and 22.0 nm, respectively, which was consistent with the above N_2O oxidation. These results suggested that the introduction of SiO_2 could improve the dispersion of Cu and inhibit the agglomeration of Cu during the reduction process.
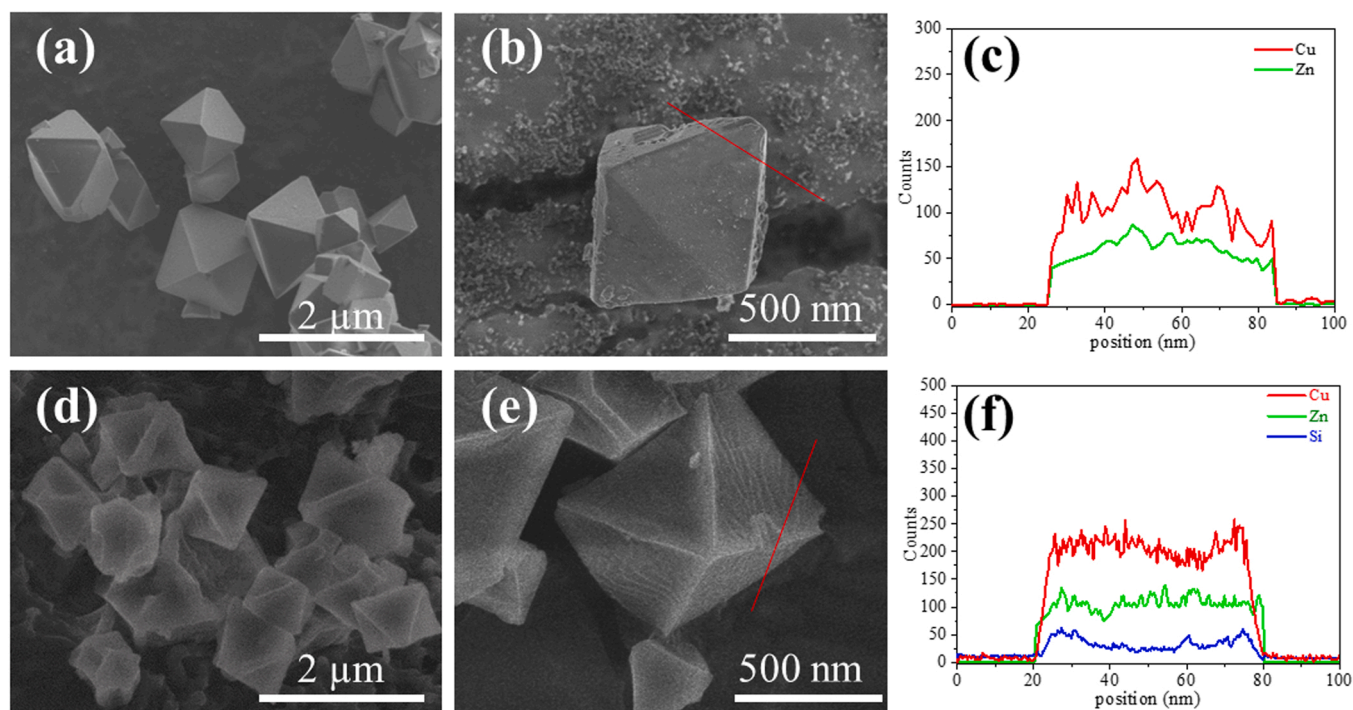
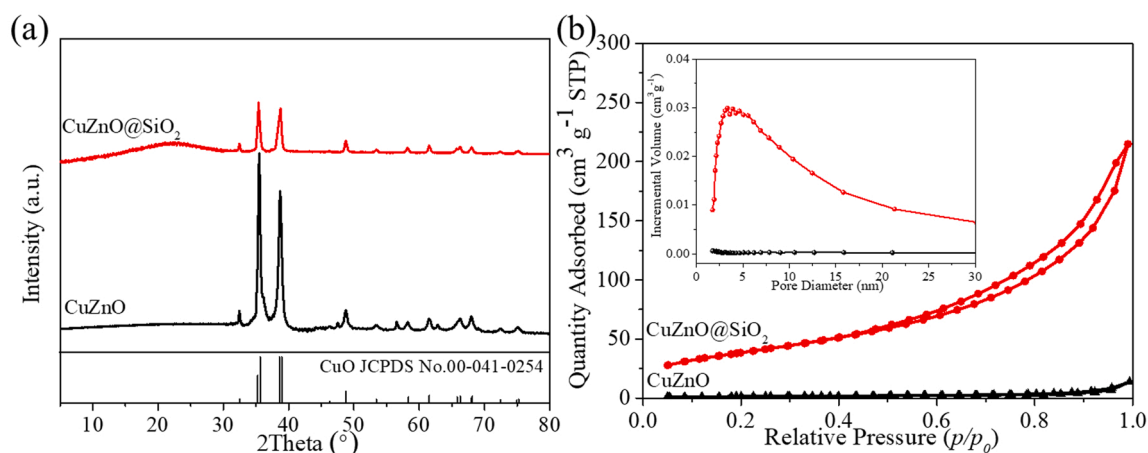**Fig. 3.** SEM images and corresponding line-EDS of CuZn-BTC (a-c) and CuZn^{BTC}@SiO$_2$ (d-f).

Fig. 4. XRD (a), N$_2$ adsorption-desorption isotherms (b) and pore size distribution (insert) of CuZnO and CuZnO@SiO$_2$.

Table 1
Textural properties of CuZnO and CuZnO@SiO$_2$.

Sample	S$_{BET}$ (m^2/g)	Pore volume (cm^3/g)[a]	Cu dispersion (%)[b]	Cu particle size (nm)[b]	Surface content[c] (%)	Bulk content[d] (%)
CuZnO	5.3	0.02	3.5	22.2	45.5	39.6
CuZnO@SiO$_2$	139.7	0.33	20.4	4.9	11.8	30.0
CuZnO@SiO$_2$[e]	112.4	0.30	17.0	5.9	10.6	30.1

[a] Calculated in Barrett-Joyner-Halenda method.
[b] Calculated from N$_2$O titration (at 30 °C) after the catalysts were reduced in H$_2$ at 350 °C.
[c] Data from XPS analysis.
[d] Data from ICP analysis.
[e] Spent CuZnO@SiO$_2$ after time on stream for 200 h at 350 °C.

Fig. 6(a) revealed the TEM images of Cu/ZnO@SiO$_2$, which confirmed the octahedral profile was still maintained in reduced Cu/ZnO@SiO$_2$. Meanwhile, both the elemental mapping of a separated octahedral particle (see Fig. 6(a)) and the line-scanning elemental analysis of enlarged images (see Fig. 6(b) and (d)) indicated that an octahedral shaped SiO$_2$ hollow formed in Cu/ZnO@SiO$_2$ catalyst, and most Cu/ZnO particles were encapsulated in SiO$_2$ hollow. More interestingly, HAADF image and corresponding line-scanning elemental
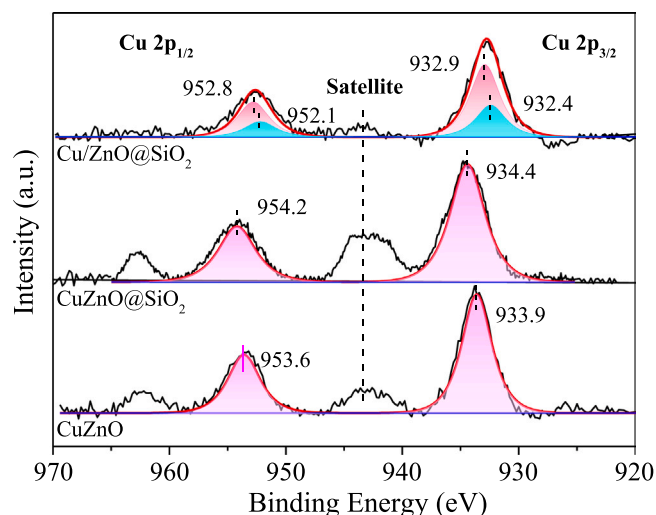
Fig. 5. Binding energies of Cu 2p in CuZnO, CuZnO@SiO$_2$ and Cu/ZnO@SiO$_2$.

analysis (see Fig. 6(d)), the fast Fourier transformation (FFT) analysis of HRTEM images with the lattice plane intensity profile (see Fig. 6(e)-(g)) disclosed that those reduced Cu particles (sized in 4–5 nm) were dotted with even smaller ZnO particles (sized in 1–2 nm). The interplanar spacing of the pure copper phase is 0.258 nm (110) (see Fig. 6(e)-(f)), and the interplanar spacing of ZnO is 0.241 nm (101) [21,43] (see Fig. 6 (e)-(g)).

3.4. Catalytic performance

Table S2 compared the performance of reference ZnO@SiO$_2$ and Cu@SiO$_2$ catalysts for the dehydrogenation of ethanol in a vertical fixed-bed reactor at 310 °C. It was found that (1) ZnO@SiO$_2$ was inactive for this reaction, (2) Cu@SiO$_2$ was active for the dehydrogenation with a moderate conversion of ethanol (40.1%) and (3) the conversion of ethanol reached 84.2% over Cu/ZnO@SiO$_2$ under the same reaction conditions. These results confirmed that Cu was indispensable for the dehydrogenation of ethanol. At the same time, the higher activity of Cu/ZnO@SiO$_2$ than that of Cu@SiO$_2$ further indicated that ZnO could improve the activity of Cu for the dehydrogenation of ethanol. The promotion effect of ZnO on the performance of Cu-based catalysts were also reported in methanol synthesis [44–46], methanol decomposition, steam reforming and partial oxidation to hydrogen [47].

Table 2 summarized the initial performance of Cu/ZnO@SiO$_2$ and Cu/ZnO (prepared via the direct calcination and reduction of pristine CuZn-BTC without SiO$_2$) for the continuous dehydrogenation of ethanol at 310 °C. It was found that the conversion of ethanol over Cu/ZnO was 75.9%, and selectivity of acetaldehyde reached 98.2%. Under the same conditions, Cu/ZnO@SiO$_2$ exhibited better performance than that of Cu/ZnO, and the detected conversion of ethanol and selectivity of acetaldehyde increased to 84.2% and 99.1%, respectively. The calculated space time yield (STY) of acetaldehyde over Cu/ZnO@SiO$_2$ reached 8.1 g-AcH/g-cat/h at 310 °C. This improvement might benefit from the high specific surface area and high dispersion of copper in Cu/ZnO@SiO$_2$. In addition, Fig. S6 compared the stability of Cu/ZnO and Cu/ZnO@SiO$_2$ for the dehydrogenation of ethanol at 310 °C. It was found that the Cu/ZnO deactivated quickly as the detected conversion of ethanol decreased sharply to 40.1% (within 40 h). On the other hand, it was interesting to note that Cu/ZnO@SiO$_2$ could maintain its activity for 50 h, mainly thanks to that Cu/ZnO were further encapsulated in SiO$_2$ hollow. The advantages of SiO$_2$ modified catalyst could be attributed to its high surface area and stabilized catalyst structure.

The performance of Cu/ZnO@SiO$_2$ for dehydrogenation of ethanol under varied reaction temperature (250–390 °C) was shown in Fig. 7. It was found the conversion of ethanol was limited (50.6%) at lower temperature (250 °C) and it increased quickly to 84.2% (at 310 °C), after that, the conversion of ethanol increased slowly to 91.2% (at 350 °C) and 93.8% (at 390 °C). On the other hand, the selectivity of acetaldehyde decreased slightly from 99.6% (at 250 °C) to 98.0% (at 390 °C), which might be attributed to the highly reactivity of acetaldehyde [48].

Fig. S7 exhibited the performance of Cu/ZnO@SiO$_2$ for the dehydrogenation of ethanol under different contact time at 310 °C. It was found that the detected conversion of ethanol increased rapidly from 30.9% (at 0.06 h) to 84.2% (at 0.32 h), and remained higher than 85% under the prolonged contact time. However, the selectivity for acetaldehyde decreased slightly under longer contact time due to the reactivity of acetaldehyde.

The stability of Cu/ZnO@SiO$_2$ catalyst for the dehydrogenation of ethanol was checked under extremely harsh condition (350 °C) (see Fig. 8). At first, it was confirmed Cu/ZnO@SiO$_2$ was stable at 310 °C within 50 h as the detected conversion of ethanol changed slightly around 84%. After that, the conversion of ethanol could be increased to 88% and remained stable within another 50 h when the temperature was raised to 330 °C. Finally, the temperature was increased to 350 °C in order to accelerate the deactivation of Cu/ZnO@SiO$_2$. It was quite interesting to note that the detected conversion of ethanol only decreased slightly from 91.2% to 90.1% within the followed 200 h. And the selectivity of acetaldehyde remained higher than 98.5% within all these 300 h. To the best of our knowledge, this prominent stability of Cu-based catalyst at high temperature (350 °C) for the dehydrogenation of ethanol was seldom reported in literatures. Characterization results indicated that Cu and ZnO particles still dispersed homogenously in spent catalyst with a slightly increased size (see Figs. S8 and S9 and Table 1). But the octahedral profile collapsed partially (see Fig. S8), which might be attributed to the violent mechanical treatments of spent Cu/ZnO@SiO$_2$. These destructive treatments include tablet compressing (before reaction), scouring of hot gas (350 °C, 200 h) and grinding (before TEM analysis). According to above characterization results, the stability of Cu/ZnO@SiO$_2$ could be attributed to the following reasons: (1) Cu and Zn dispersed homogenously in its precursor (CuZn^{BTC}@SiO$_2$, see Fig. 3b), and (2) those Cu particles (4–5 nm) were dotted with fine ZnO particles in the final catalyst which could make Cu particle isolated from each other (see Fig. 6(d)&(e)). At last, (3) SiO$_2$ hollow could also protect the sintering of these Cu/ZnO particles. These results confirmed that Cu/ZnO@SiO$_2$ is an excellent catalyst for the dehydrogenation of ethanol compared with those published works for its higher STY and stability (see Table S3 for details) [21,23,49–53].

4. Conclusions

In conclusion, a stable Cu-based catalyst was prepared via the controlled calcination and reduction of a silica encapsulated CuZn-BTC. Characterization results indicated that SiO$_2$ could prevent the violent burning of organic linkers during calcination, retard the sintering of Cu/ZnO particles. The final Cu/ZnO@SiO$_2$ catalyst possesses increased surface area, highly dispersed Cu particles and most Cu particles were dotted and isolated with fine ZnO. At the same time, SiO$_2$ hollow could also protect the sintering of these Cu/ZnO hybrids. As a result, Cu/ZnO@SiO$_2$ catalyst exhibited prominent activity and stability for the dehydrogenation of ethanol. The selectivity and STY of acetaldehyde reached 98.5% and 9.0 g-acetaldehyde/g-cat/h, respectively, at 350 °C, 0.1 MPa and WHSV = 3.1 h^{-1}. Meanwhile, Cu/ZnO@SiO$_2$ could maintain its activity within 200 h on stream in a severe condition (350 °C). This strategy will improve the lifetime of Cu-based catalysts under harsher conditions and broaden their application in the field of heterogeneous catalysis.
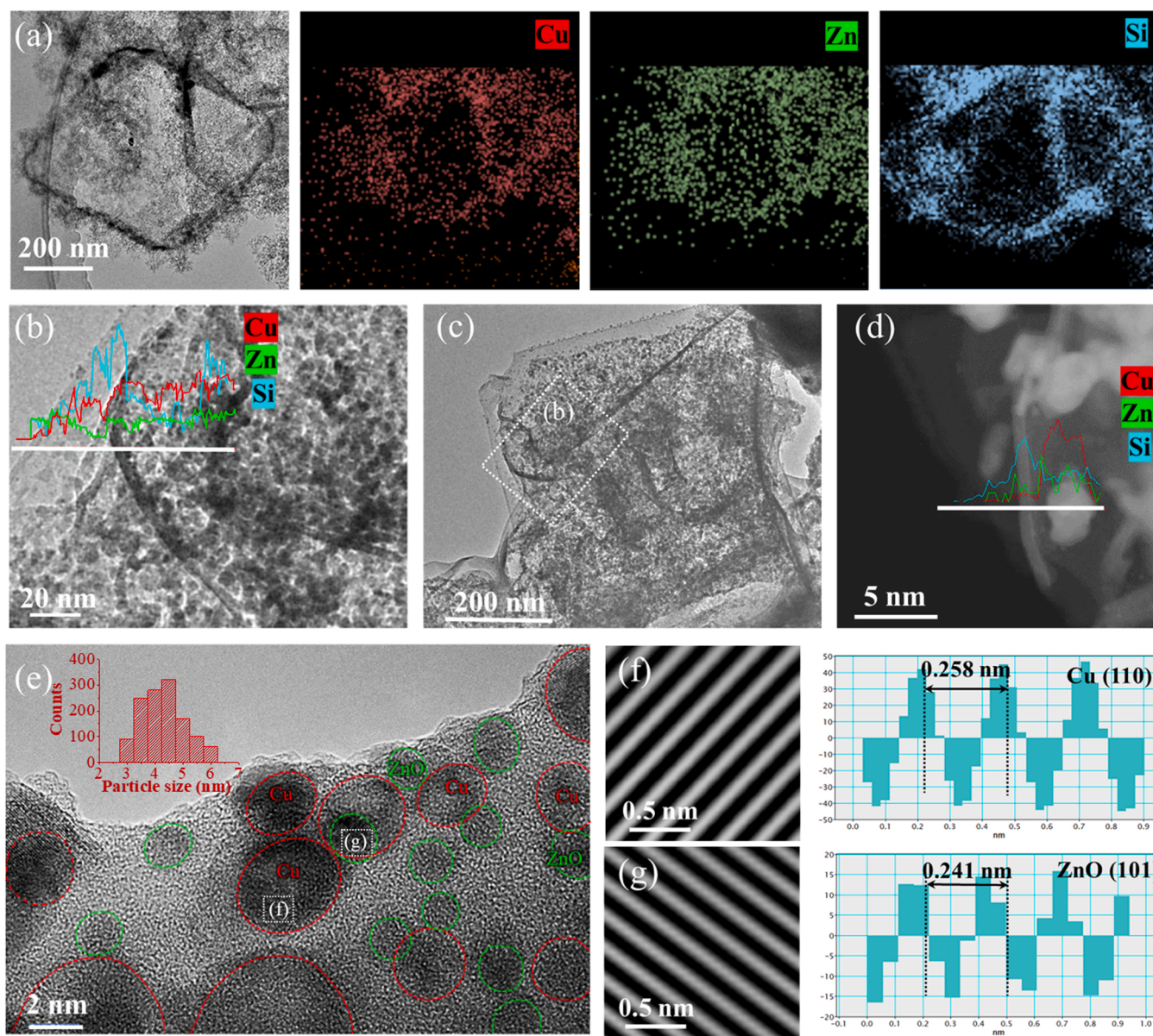
Fig. 6. HRTEM images (a, b, c, e) and the HAADF image (d) of Cu/ZnO@SiO$_2$; the fast Fourier transformation (FFT) of the HRTEM images (f, g) with the lattice plane intensity profile.

Table 2
Dehydrogenation of ethanol over Cu/ZnO and Cu/ZnO@SiO$_2$.

Catalyst	Conv. (%)	Selectivity (%)					STY (g-AcH/g-cat/h)[a]
		AcH[b]	EtOAc[c]	HOAc[d]	Et$_2$O[e]	Others[f]	
Cu/ZnO	75.9	98.2	0.4	0.2	0.6	0.6	7.5
Cu/ZnO@SiO$_2$	84.2	99.1	0.3	–	0.4	0.2	8.1

Reaction conditions: catalyst 0.3 g; 310 °C; 0.1 MPa, 20 mL/min N$_2$; ethanol feed in 1.2 mL/h, WHSV = 3.2 h^{-1}.

[a] STY, defined as (gram of formed acetaldehyde)/ (gram of catalyst)/ (contact time).
[b] AcH, acetaldehyde.
[c] EtOAc, ethyl acetate.
[d] HOAc, acetic acid.
[e] Et$_2$O, diethyl ether.
[f] Others, mainly containing acetaldehyde oligomer.

CRediT authorship contribution statement

Haolan Liu: Investigation, Methodology, Formal analysis, Writing - Original Draft. **Zhili Chang**: Investigation, Validation, Formal analysis. **Jie Fu**: Discussion, Supervision, Funding acquisition. **Zhaoyin Hou**: Conceptualization, Resources, Writing - Review & Editing, Supervision, Funding acquisition.
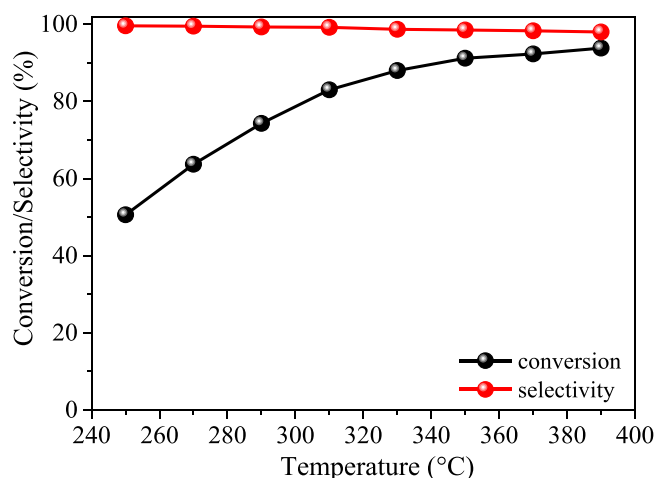
Fig. 7. Dehydrogenation of ethanol over Cu/ZnO@SiO$_2$ at varied temperature. Reaction conditions: catalyst 0.3 g; 0.1 MPa, 20 mL/min N$_2$; ethanol feed 1.2 mL/h, WHSV= 3.2 h^{-1}.
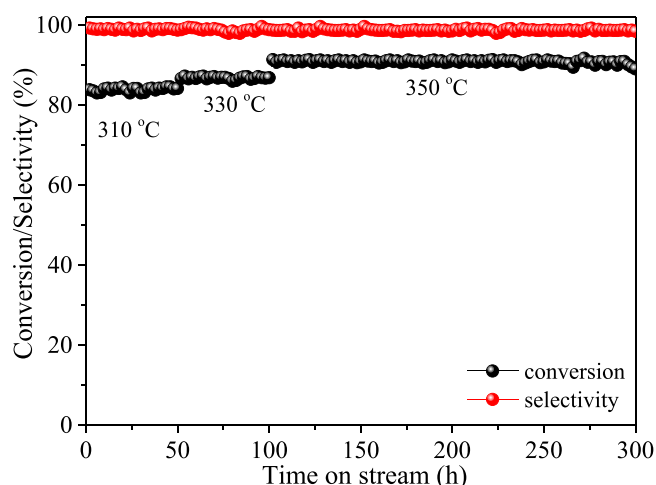

Fig. 8. Stability of Cu/ZnO@SiO$_2$ for the dehydrogenation of ethanol. Reaction conditions: catalyst 0.3 g; 0.1 MPa, 20 mL/min N$_2$; ethanol with feed of 1.2 mL/h, WHSV= 3.2 h^{-1}.

Declaration of Competing Interest

The authors declare that they have no known competing financial interests or personal relationships that could have appeared to influence the work reported in this paper.

Data availability

Data will be made available on request.

Appendix A. Supporting information

Supplementary data associated with this article can be found in the online version at doi:10.1016/j.apcatb.2022.122194.

References

[1] N.M. Eagan, M.D. Kumbhalkar, J.S. Buchanan, J.A. Dumesic, G.W. Huber, Chemistries and processes for the conversion of ethanol into middle-distillate fuels, Nat. Rev. Chem. 3 (2019) 223–249.

[2] L. Qi, Y. Zhang, M.A. Conrad, C.K. Russell, J. Miller, A.T. Bell, Ethanol conversion to butadiene over isolated zinc and yttrium sites grafted onto dealuminated beta zeolite, J. Am. Chem. Soc. 142 (2020) 14674–14687.

[3] S. Subramaniam, M.F. Guo, T. Bathena, M. Gray, X. Zhang, A. Martinez, L. Kovarik, K.A. Goulas, K.K. Ramasamy, Direct catalytic conversion of ethanol to C$_{5+}$ ketones: role of Pd-Zn alloy on catalytic activity and stability, Angew. Chem. Int. Ed. 59 (2020) 14550–14557.

[4] J. Pang, M. Yin, P. Wu, X. Li, H. Li, M. Zheng, T. Zhang, Advances in catalytic dehydrogenation of ethanol to acetaldehyde, Green Chem. 23 (2021) 7902–7916.

[5] G. Giannakakis, P. Kress, K. Duanmu, H.T. Ngan, G. Yan, A.S. Hoffman, Z. Qi, A. Trimpalis, L. Annamalai, M. Ouyang, J. Liu, N. Eagan, J. Biener, D. Sokaras, M. Flytzani-Stephanopoulos, S.R. Bare, P. Sautet, E.C.H. Sykes, Mechanistic and electronic insights into a working NiAu single-atom alloy ethanol dehydrogenation catalyst, J. Am. Chem. Soc. 143 (2021) 21567–21579.

[6] M. Ouyang, K.G. Papanikolaou, A. Boubnov, A.S. Hoffman, G. Giannakakis, S. R. Bare, M. Stamatakis, M. Flytzani-Stephanopoulos, E.C.H. Sykes, Directing reaction pathways via in situ control of active site geometries in PdAu single-atom alloy catalysts, Nat. Commun. 12 (2021) 1549.

[7] R. Jira, Acetaldehyde from ethylene-a retrospective on the discovery of the wacker process, Angew. Chem. Int. Ed. 48 (2009) 9034–9037.

[8] J.A. Keith, P.M. Henry, The mechanism of the wacker reaction: a tale of two hydroxypalladations, Angew. Chem. Int. Ed. 48 (2009) 9038–9049.

[9] S. Hanukovich, A. Dang, P. Christopher, Influence of metal oxide support acid sites on Cu-catalyzed nonoxidative dehydrogenation of ethanol to acetaldehyde, ACS Catal. 9 (2019) 3537–3550.

[10] Q. Yang, X. Huang, J. Zhang, Z. Xiao, X. Duan, S. Zhou, Y. Niu, H. Sun, L. Zhi, S. Wang, Unzipping MWCNTs for controlled edge- and heteroatom-defects in revealing their roles in gas-phase oxidative dehydrogenation of ethanol to acetaldehyde, Chem. Eng. J. 446 (2022) 137150.

[11] S. Kondaveeti, G.D. Park, R. Shanmugam, R. Pagolu, S.K.S. Patel, A. Bisht, D. R. Kim, Y.C. Kang, J.-K. Lee, Investigating the role of metals loaded on nitrogen-doped carbon-nanotube electrodes in electroenzymatic alcohol dehydrogenation, Appl. Catal. B: Environ. 307 (2022), 121195.

[12] P. García-Muñoz, N.P. Zussblatt, B.F. Chmelka, V.A. de la Peña O'Shea, F. Fresno, Production of hydrogen from gas-phase ethanol dehydrogenation over iron-grafted mesoporous Pt/TiO$_2$ photocatalysts, Chem. Eng. J. 450 (2022), 138450.

[13] H. Liu, Y. Jiang, R. Zhou, Z. Chang, Z. Hou, Co-production of hydrogen and acetaldehyde from ethanol over a highly dispersed Cu catalyst, Fuel 321 (2022), 123980.

[14] D. Gao, Y. Feng, H. Yin, A. Wang, T. Jiang, Coupling reaction between ethanol dehydrogenation and maleic anhydride hydrogenation catalyzed by Cu/Al$_2$O$_3$, Cu/ZrO$_2$, and Cu/ZnO catalysts, Chem. Eng. J. 233 (2013) 349–359.

[15] G. Pampararo, G. Garbarino, A. Comite, G. Busca, P. Riani, Acetaldehyde production by ethanol dehydrogenation over Cu-ZnAl$_2$O$_4$: effect of catalyst synthetic strategies on performances, Chem. Eng. Sci. 261 (2022), 117937.

[16] Q. Wan, F. Wei, Y. Wang, F. Wang, L. Zhou, S. Lin, D. Xie, H. Guo, Single atom detachment from Cu clusters, and diffusion and trapping on CeO$_2$(111): implications in ostwald ripening and atomic redispersion, Nanoscale 10 (2018) 17893–17901.

[17] D. Li, X. Li, J. Gong, Catalytic reforming of oxygenates: state of the art and future prospects, Chem. Rev. 116 (2016) 11529–11653.

[18] P. Zhang, Q.-N. Wang, X. Yang, D. Wang, W.-C. Li, Y. Zheng, M. Chen, A.-H. Lu, A highly porous carbon support rich in graphitic-N stabilizes copper nanocatalysts for efficient ethanol dehydrogenation, ChemCatChem 9 (2017) 505–510.

[19] C. Wang, G. Garbarino, L.F. Allard, F. Wilson, G. Busca, M. Flytzani-Stephanopoulos, Low-temperature dehydrogenation of ethanol on atomically dispersed gold supported on ZnZrO$_x$, ACS Catal. 6 (2016) 210–218.

[20] E. Santacesaria, G. Carotenuto, R. Tesser, M. Di Serio, Ethanol dehydrogenation to ethyl acetate by using copper and copper chromite catalysts, Chem. Eng. J. 179 (2012) 209–220.

[21] J. Shan, N. Janvelyan, H. Li, J. Liu, T.M. Egle, J. Ye, M.M. Biener, J. Biener, C. M. Friend, M. Flytzani-Stephanopoulos, Selective non-oxidative dehydrogenation of ethanol to acetaldehyde and hydrogen on highly dilute NiCu alloys, Appl. Catal. B: Environ. 205 (2017) 541–550.

[22] K. Ramachandran, M. Vinothkannan, A.R. Kim, S. Ramakrishnan, D.J. Yoo, Ultrafine bimetallic alloy supported on nitrogen doped reduced graphene oxide toward liquid-fuel oxidation: profile of improved performance and extended durability, Int. J. Hydrog. Energ. 44 (2019) 21769–21780.

[23] J. Pang, M. Zheng, C. Wang, X. Yang, H. Liu, X. Liu, J. Sun, Y. Wang, T. Zhang, Hierarchical echinus-like Cu-MFI catalysts for ethanol dehydrogenation, ACS Catal. 10 (2020) 13624–13629.

[24] L. Lin, P. Cao, J. Pang, Z. Wang, Q. Jiang, Y. Su, R. Chen, Z. Wu, M. Zheng, W. Luo, Zeolite-encapsulated Cu nanoparticles with enhanced performance for ethanol dehydrogenation, J. Catal. 413 (2022) 565–574.

[25] L. Jiao, J.Y.R. Seow, W.S. Skinner, Z.U. Wang, H.-L. Jiang, Metal–organic frameworks: structures and functional applications, Mater. Today 27 (2019) 43–68.

[26] Y.-Z. Chen, R. Zhang, L. Jiao, H.-L. Jiang, Metal–organic framework-derived porous materials for catalysis, Coord. Chem. Rev. 362 (2018) 1–23.

[27] H. Ye, H. Zhao, Y. Jiang, H. Liu, Z. Hou, Catalytic transfer hydrogenation of the C=O bond in unsaturated aldehydes over Pt nanoparticles embedded in porous UiO-66 nanoparticles, ACS Appl. Nano Mater. 3 (2020) 12260–12268.

[28] H. Chen, K. Shen, Q. Mao, J. Chen, Y. Li, Nanoreactor of MOF-derived yolk–shell Co@C-N: precisely controllable structure and enhanced catalytic activity, ACS Catal. 8 (2018) 1417–1426.

[29] J. Lin, C. Zeng, X. Lin, C. Xu, C.-Y. Su, CNT-assembled octahedron carbon-encapsulated Cu$_3$P/Cu heterostructure by in situ MOF-derived engineering for superior lithium storage: investigations by experimental implementation and first-principles calculation, Adv. Sci. 7 (2020), 2000736.

[30] Y. Yang, Y. Huang, S. Zhou, Y. Liu, L. Shi, T.T. Isimjan, X. Yang, Delicate surface vacancies engineering of Ru doped MOF-derived Ni-NiO@C hollow microsphere superstructure to achieve outstanding hydrogen oxidation performance, J. Energy Chem. 72 (2022) 395–404.

[31] L. Zheng, X. Li, W. Du, D. Shi, W. Ning, X. Lu, Z. Hou, Metal-organic framework derived Cu/ZnO catalysts for continuous hydrogenolysis of glycerol, Appl. Catal. B: Environ. 203 (2017) 146–153.

[32] H. Zhao, Y. Jiang, P. Chen, J. Fu, X. Lu, Z. Hou, CoZn-ZIF-derived ZnCo$_2$O$_4$-framework for the synthesis of alcohols from glycerol, Green Chem. 20 (2018) 4299–4307.

[33] H. Zhao, Y. Jiang, H. Liu, Y. Long, Z. Wang, Z. Hou, Direct synthesis of allyl alcohol from glycerol over CoFe alloy, Appl. Catal. B: Environ. 277 (2020), 119187.

[34] W. Xu, Y. Zhang, J. Wang, Y. Xu, L. Bian, Q. Ju, Y. Wang, Z. Fang, Defects engineering simultaneously enhances activity and recyclability of MOFs in selective hydrogenation of biomass, Nat. Commun. 13 (2022) 2068.

[35] J. Zhao, W.T. Nunn, P.C. Lemaire, Y. Lin, M.D. Dickey, C.J. Oldham, H.J. Walls, G. W. Peterson, M.D. Losego, G.N. Parsons, Facile conversion of hydroxy double salts to metal-organic frameworks using metal oxide particles and atomic layer deposition thin-film templates, J. Am. Chem. Soc. 137 (2015) 13756–13759.

[36] T. Qi, Y. Zhao, S. Chen, W. Li, X. Guo, Y. Zhang, C. Song, Bimetallic metal organic framework-templated synthesis of a Cu-ZnO/Al$_2$O$_3$ catalyst with superior methanol selectivity for CO$_2$ hydrogenation, Mol. Catal. 514 (2021) 111870.

[37] H. Shankar, W.W. Yu, Y. Kang, P. Kar, Significant boost of the stability and PLQY of CsPbBr$_3$ NCs by Cu-BTC MOF, Sci. Rep. 12 (2022) 7848.

[38] T. Shen, T. Liu, H. Mo, Z. Yuan, F. Cui, Y. Jin, X. Chen, Cu-based metal-organic framework HKUST-1 as effective catalyst for highly sensitive determination of ascorbic acid, RSC Adv. 10 (2020) 22881–22890.

[39] X. Jiang, Y. Chen, M.U. Nisa, X. Li, N. Zhao, Z. Li, Highly active Fe$_x$O$_y$@SiO$_2$ catalyst for fischer-tropsch synthesis through the confinement effect of metal organic frameworks material: preparation and structure-activity relationship, Mol. Catal. 513 (2021) 111813.

[40] J. Sun, M. Shang, M. Zhang, S. Yu, Z. Yuan, X. Yi, S. Filatov, J. Zhang, Konjac glucomannan/cellulose nanofibers composite aerogel supported HKUST-1 for CO$_2$ adsorption, Carbohydr. Polym. 293 (2022), 119720.

[41] K. Liu, S. Jiao, H. Zhao, F. Cao, D. Ma, Hybridization of MOFs and ionic POFs: a new strategy for the construction of bifunctional catalysts for CO$_2$ cycloaddition, Green Chem. 23 (2021) 1766–1771.

[42] J. Schumann, M. Eichelbaum, T. Lunkenbein, N. Thomas, M.C. Álvarez Galván, R. Schlögl, M. Behrens, Promoting strong metal support interaction: doping ZnO for enhanced activity of Cu/ZnO:M (M = Al, Ga, Mg) catalysts, ACS Catal. 5 (2015) 3260–3270.

[43] L. Xue, C. Zhang, T. Shi, S. Liu, H. Zhang, M. Sun, F. Liu, Y. Liu, Y. Wang, X. Gu, S. Zeng, Unraveling the improved CO$_2$ adsorption and COOH* formation over Cu-decorated ZnO nanosheets for CO$_2$ reduction toward CO, Chem. Eng. J. (2022), 139701.

[44] M. Behrens, F. Studt, I. Kasatkin, S. Kühl, M. Hävecker, F. Abild-Pedersen, S. Zander, F. Girgsdies, P. Kurr, B.-L. Kniep, M. Tovar, R.W. Fischer, J.K. Nørskov, R. Schlögl, The active site of methanol synthesis over Cu/ZnO/Al$_2$O$_3$ industrial catalysts, Science 336 (2012) 893–897.

[45] S. Kuld, M. Thorhauge, H. Falsig, C.F. Elkjær, S. Helveg, I. Chorkendorff, J. Sehested, Quantifying the promotion of Cu catalysts by ZnO for methanol synthesis, Science 352 (2016) 969–974.

[46] S. Kattel, P.J. Ramírez, J.G. Chen, J.A. Rodriguez, P. Liu, Active sites for CO$_2$ hydrogenation to methanol on Cu/ZnO catalysts, Science 355 (2017) 1296–1299.

[47] L. Mo, A.H. Wan, X. Zheng, C.-T. Yeh, Selective production of hydrogen from partial oxidation of methanol over supported silver catalysts prepared by method of redox coprecipitation, Catal. Today 148 (2009) 124–129.

[48] S.J. Raynes, R.A. Taylor, Zinc oxide-modified mordenite as an effective catalyst for the dehydrogenation of (bio)ethanol to acetaldehyde, Sustain. Energ. Fuels 5 (2021) 2136–2148.

[49] A.G. Sato, D.P. Volanti, D.M. Meira, S. Damyanova, E. Longo, J.M.C. Bueno, Effect of the ZrO$_2$ phase on the structure and behavior of supported Cu catalysts for ethanol conversion, J. Catal. 307 (2013) 1–17.

[50] S. Tayrabekova, P. Mäki-Arvela, M. Peurla, P. Paturi, K. Eränen, G.E. Ergazieva, A. Aho, D.Y. Murzin, K. Dossumov, Catalytic dehydrogenation of ethanol into acetaldehyde and isobutanol using mono- and multicomponent copper catalysts, C. R. Chim. 21 (2018) 194–209.

[51] H. Zhang, H.-R. Tan, S. Jaenicke, G.-K. Chuah, Highly efficient and robust Cu catalyst for non-oxidative dehydrogenation of ethanol to acetaldehyde and hydrogen, J. Catal. 389 (2020) 19–28.

[52] M.-Y. Li, W.-D. Lu, L. He, F. Schüth, A.-H. Lu, Tailoring the surface structure of silicon carbide support for copper catalyzed ethanol dehydrogenation, ChemCatChem 11 (2018) 481–487.

[53] Q.-N. Wang, L. Shi, W. Li, W.-C. Li, R. Si, F. Schüth, A.-H. Lu, Cu supported on thin carbon layer-coated porous SiO$_2$ for efficient ethanol dehydrogenation, Catal. Sci. Technol. 8 (2018) 472–479.